Editors' Suggestion

RETRACTED: Colossal Density-Driven Resistance Response in the Negative Charge Transfer Insulator MnS_2

Dylan Durkee,[1,§] Nathan Dasenbrock-Gammon,[2] G. Alexander Smith,[3] Elliot Snider,[4] Dean Smith,[1,5] Christian Childs,[1] Simon A. J. Kimber,[6] Keith V. Lawler,[3,*] Ranga P. Dias,[2,4,†] and Ashkan Salamat[1,‡]

[1]*Department of Physics & Astronomy, University of Nevada Las Vegas, Las Vegas, Nevada 89154, USA*
[2]*Department of Physics & Astronomy, University of Rochester, Rochester, New York 14627, USA*
[3]*Department of Chemistry & Biochemistry, University of Nevada Las Vegas, Las Vegas, Nevada 89154, USA*
[4]*Department of Mechanical Engineering, University of Rochester, Rochester, New York 14627, USA*
[5]*HPCAT, X-ray Science Division, Argonne National Laboratory, Argonne, Illinois 60439, USA*
[6]*Université Bourgogne Franche-Comté, Université de Bourgogne, ICB-Laboratoire Interdisciplinaire Carnot de Bourgogne, Bâtiment Sciences Mirande, 9 Avenue Alain Savary, B-P. 47870, 21078 Dijon Cedex, France*

(Received 9 February 2021; revised 8 April 2021; accepted 4 June 2021; published 30 June 2021)

A reversible density driven insulator to metal to insulator transition in high-spin MnS_2 is experimentally observed, leading with a colossal electrical resistance drop of 10^8 Ω by 12 GPa. Density functional theory simulations reveal the metallization to be unexpectedly driven by previously unoccupied S_2^{2-} σ^*_{3p} antibonding states crossing the Fermi level. This is a unique variant of the charge transfer insulator to metal transition for negative charge transfer insulators having anions with an unsaturated valence. By 36 GPa the emergence of the low-spin insulating arsenopyrite ($P2_1/c$) is confirmed, and the bulk metallicity is broken with the system returning to an insulative electronic state.

DOI: 10.1103/PhysRevLett.127.016401

Mott and charge-transfer insulators are materials where strong electron correlation localize partially filled levels, usually d or f, that would be itinerant according to band theory [1–3]. Such systems are highly sensitive, and hence tunable, with pressure and temperature perturbations, often revealing superconducting states, spin electronics, and the ability to overcome the energetic gap and undergo insulator to metallic transitions [4–6]. Transition metal chalcogenides (TMC) present a large and diverse family of compounds that often exhibit these complex responses under density changes, undergoing transformations to dramatically different electronic and magnetic states [7–11]. The observation of colossal electroresistance under low voltage in TMCs along with rapid, reversible, phase changes between crystalline and disordered states have led to Mott memory devices and the possibility of using pressure to tune between states is an important direction for the next-generation data storage [12]. Similar response dynamics have recently been demonstrated under high pressure conditions in amorphous metallic alloys [13].

Within the Mn chalcogenides, materials like $MnTe_2$, MnS, MnSe, $MnPS_2$, and MnS_2 all undergo exceptionally large volume collapse transitions which influence the electronic band structure [14–16]. Such responses are in part a consequence of these materials being very soft, with bulk moduli of the order of 65 GPa. In the similarly soft pnictide materials, high pressure conditions cause significant changes to the structural ground state, resulting from a degree of deviatoric stress present in the sample environment. For example, in $CaFe_2As_2$, superconductivity is seen in nonhydrostatic experiments [17], but is absent in hydrostatic conditions [18]. Diffraction experiments performed under varying conditions show that this is a result of phase coexistence induced by nonhydrostatic strain [19]. Pressure-induced metallization (PIM) driven by deviatoric stress, in TMC compounds such as MoS_2 and ReS_2 show great promise for topological materials [20,21]. Such PIM transitions also arise in other sulfide compounds, i.e., CS_2 and OCS [22,23]. Most notably, the recent confirmation of room temperature superconductivity, under pressure, in a carbonaceous sulfur hydride system highlights the dominant role sulfur seems to play in permitting the tailoring of exotic electronic transitions under extreme conditions [24].

MnS_2 is a TMC insulator with a high-spin ($S_{Mn} = 5/2$) pyrite phase ($Pa\bar{3}$, p-MnS_2) and a low-spin, ($S_{Mn} = 1/2$) high-pressure arsenopyrite ($P2_1/c$, a-MnS_2) phase [15,25]. This crystal-field driven phase transition leads to the largest reported volume collapse in any system of ∼22% [15]. Despite both phases of MnS_2 exhibiting Mott-like electronic structures [15,26,27], an insulator to metal transition has not been directly observed for either. Here we report pressure induced metallization of p-MnS_2 by 12 GPa, following a colossal drop in electrical resistance of ∼6.7 kΩ/GPa. Further compression to 36 GPa, at 300 K, reveals a spin transition into the dense arsenopyrite phase, as confirmed by *in situ* synchrotron x-ray diffraction, revealing a giant volume collapse as observed at lower pressures through thermal annealing. This high

density phase is nonmetallic and reveals that the spin transition promotes electron localization effects that break the metallicity. All transitions are fully reversible to ambient conditions.

A total of 10 high pressure experiments were conducted on MnS_2 (natural specimen) in home-designed diamond anvil cells (DACs) using 300 micron culet diamonds, up to a maximum pressure of 70 GPa. Four-probe electrical resistance measurements were carried out at room and low temperature conditions. Raman spectroscopy was conducted under nonhydrostatic and quasihydrostatic conditions, using NaCl and He as pressure transmitting media, respectively. Synchrotron x-ray diffraction (XRD) measurements were conducted under nonhydrostatic conditions at Sector 16, ID-B, HPCAT at the Advanced Photon Source ($\lambda = 0.4066$ Å). Samples were annealed at high pressure using an in-house CO_2 laser, and measured post-heating using all three experimental techniques. Density functional theory (DFT) simulations were done with VASP using the PBEsol + U [28,29] ($U_{\text{eff}} = 3.9$ eV) [30,31] functional. Further details are in the Supplemental Material [32].

The effect of pressure on MnS_2 is incredibly pronounced. Our high pressure four-probe electrical resistance measurements reveal a seven order drop in resistance within the $Pa\bar{3}$ phase [Fig. 1(a)]. By 12 GPa the system enters a metallic state as confirmed by the temperature-dependent electrical resistance, as resistance continues to decrease with a lowering in temperature [Fig. 1(b)]. At room temperature, compression above 12 GPa leads to a loss of the Raman signal of MnS_2 in both hydrostatic and nonhydrostatic conditions [Fig. 2(b)]. The loss of Raman signal under high pressure often is attributed to two distinct transitions; pressure induced amorphization (PIA) or disordering, and pressure induced metallization. Our XRD study reveals crystallinity throughout the full compression range, up to 52 GPa (Fig. 2, bottom). As amorphization is not observed, a pressure-induced insulator to metal transition can explain the loss of Raman features as the transition to a metallic state leads to a more isotropic Fermi surface and decreases inelastic electronic scattering, leading to a very weak and smeared Raman signal.

Our DFT modeling of high-spin p-MnS_2 under compression confirms antiferromagnetic type-III (AFM-III) ordering for the spins of the fcc Mn sublattice [15]. The magnetic unit cell of AFM-III p-MnS_2 is a doubled structural unit cell in the direction parallel to the spin dipoles [48,49]. There is increased crystal field splitting between the Mn t_{2g} and e_g occupied states with pressure as seen in Figs. 3(a)–3(c). It is important to note that there is a consistent higher pressure difference of ~20 GPa from our DFT work compared to our experimental results. This is a consequence of the calculations sampling a perfect crystal under hydrostatic strain at 0 K, while in contrast the experiment is conducted under nonhydrostatic conditions which provides access to lower thermodynamic barriers via

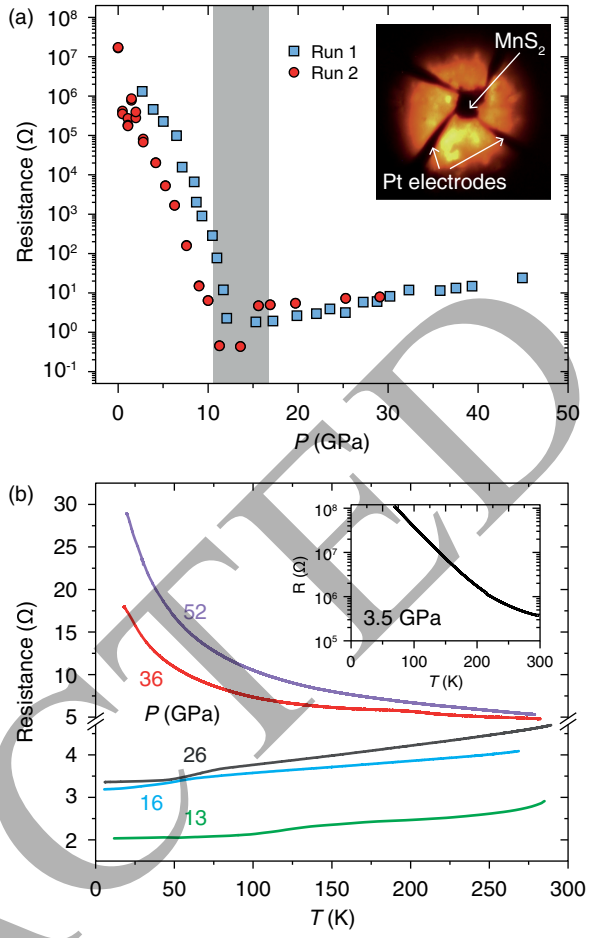

FIG. 1. (a) Electrical resistance measured across MnS_2 on compression to 52 GPa at room temperature in two independent runs. Note the greater than seven order magnitude drop in resistance measured across the six different electrode pair combinations. (inset) Microscope image of the sample loading showing the position of the leads in the sample chamber. (b) 5 independent low temperature runs at fixed pressure. (inset) Resistance curve at 3.5 GPa.

nonequilibrium pathways. The crystal field splitting with pressure drives the top states of the valence band to separate from the rest of the valence band. The isolated valence band is composed of 2 spin bands per Mn, primarily representing the two half occupied e_g states per Mn. The Mn e_g character of those bands increases with pressure, but they still exhibit some S p character at the highest pressures evaluated.

Band structure calculations reveal the onset of metallization begins (~30 GPa) when the conduction band takes on a small partial occupancy in the vicinity of the Γ-point despite a 0.185 eV direct band gap at Γ. The dispersion of the valence states increases with pressure while the separation between the valence and conduction bands decreases, indicating that the measured drop in resistance has Mott-like characteristics. Actual metallization and disappearance of the gap occurs when the conduction band minimum (CBM) migrates below the Fermi level near the Γ

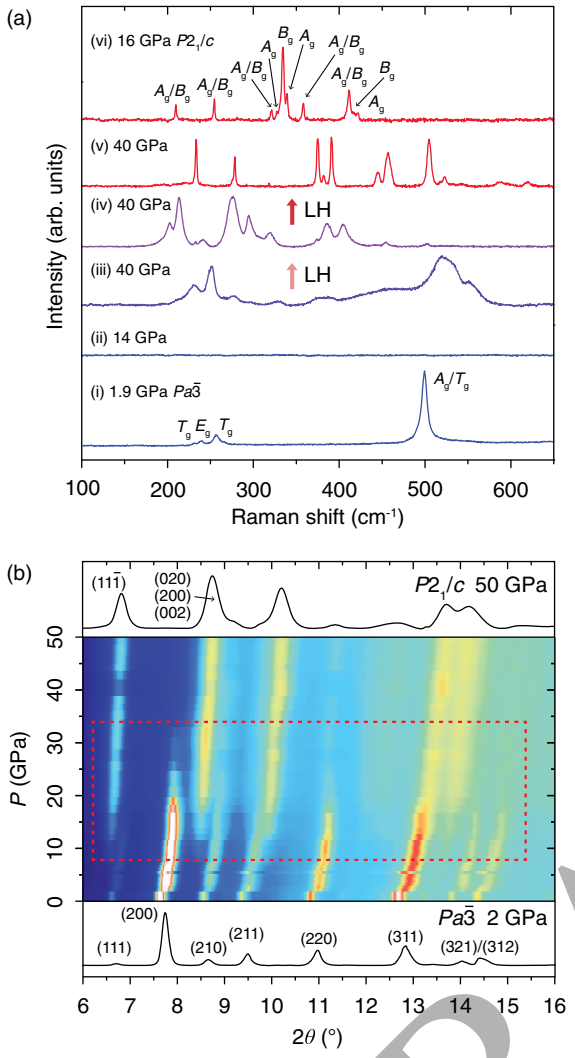

FIG. 2. (a) Raman spectra of MnS_2 under different conditions showing (i) the back transformation to the ambient $Pa\bar{3}$ pyrite phase on decompression from 52 GPa; (ii) disappearance of the signal by 14 GPa under nonhydrostatic compression; (iii) emergence of a new signal after nonhydrostatic compression to 52 GPa followed by decompression to 40 GPa; (iv) mixed phases after CO_2 laser heating the sample from (iii) at 40 GPa with low laser power; (v) concentration of $P2_1/c$ after further CO_2 laser heating; and (vi) $P2_1/c$ signal after laser heating a hydrostatic sample at 16 GPa for comparison. (b) XRD density plot of MnS_2 with pressure. Red dashed lines emphasize the pressure region (10–36 GPa) of mixed phases. Distinct pyrite peaks are seen below 10 GPa, as well as distinct arsenopyrite peaks above 36 GPa.

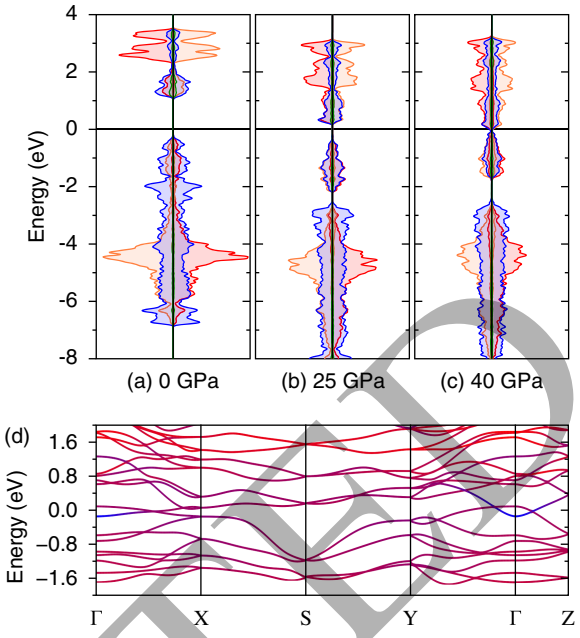

FIG. 3. (a),(b),(c) Pressure dependence of the projected density of states (right: spin-up, left: spin-down) for high-spin AFM-III pyrite(-like) MnS_2: Mn d on atoms with $\mu_B > 0$ (red), Mn d on atoms with $\mu_B < 0$ (orange), S p (blue), and S s (green). (d) The Mn d (red) and S p (blue) components projected onto the spin-up bands near the Fermi level for high-spin AFM-III pyrite(-like) MnS_2 at 40 GPa.

point and switches identities with the valence band maximum (VBM) [Figs. 3(c), 3(d)]. There is a drop in the computed magnetic moment per Mn with pressure—from 4.48 μ_B at 0 GPa to 3.84 μ_B at 40 GPa. Contrary to the drop in magnetic moment, the per Mn d occupancy increases from 4.90 at 0 GPa to 5.15 at 40 GPa, while the per S p occupation also increases from 2.34 at 0 GPa to 2.42 at 40 GPa. Thus, accompanying the metallization is a non-negligible (~0.16 electron/S_2) amount of metal-to-ligand charge transfer (MLCT) from increasingly itinerant Mn d electrons.

Inspection of the band structure and density of states for high-spin p-MnS_2 shows that it is not a Mott insulator like previously prescribed [26], but rather more a negative charge transfer insulator. In this class of materials, the anion has an unsaturated valence contributing a conduction band between the metal's separated valence and conduction d bands [50–52]. When p-MnS_2 metallizes, the VBM is composed of S_2^{2-} σ^*_{3p} states and not Mn d states at Γ where the CBM and VBM cross [Fig. 3(d)]. Away from Γ the CBM and VBM retain similar compositions as at lower pressures (plots in Supplemental Material [32]). This is opposed to a typical charge-transfer insulator to metal transition wherein occupied ligand p bands merge with unoccupied metal d bands [3]. There are instances of metal-insulator transitions involving the formation of a negative charge transfer insulator via a reduction-oxidation process [53,54], yet this is the first instance we can find of this mechanism for metallization unique to strongly correlated materials bearing anions with unsaturated valences.

The DFT structural optimizations show symmetry lowering distortions as early as 5 GPa. This includes a slight breaking of $a = b$ symmetry [55] from pronounced "0 K" magnetoelastic distortions along the magnetic

propagation vector [56] (Table in Supplemental Material [32]). Although our experimental XRD cannot resolve such subtle distortions to orthorhombic $Pbc2_1$, we do observe some peak broadening. The retention of a pyritelike phase is similar to another Mn dichalcogenide, $MnTe_2$, where Mössbauer spectroscopy indicates that a pyrite structure is retained after pressure induced metallization [14]. Further compression above 36 GPa reveals a nexus of electronic and structural change in the experimental measurements. Four-probe electrical measurements show an increase in resistance with increasing pressure and a lowering of temperature. This is indicative of a semiconducting state and opposite to the electronic transition at 12 GPa; the energy-density tuning drives a metal-insulator transition. Figure 1(b) shows that for temperature cooling runs at 36 and 52 GPa, there is a greater increase and hence a larger electronic band gap with pressure, respectively. This transition is followed by a change in the spectroscopic response as the Raman signal returns with a new set of features. The return to a nonmetallic state, with a band gap, increases the polarizablity of more delocalized surface plasmons, which leads to the reemergence of the Raman spectra above 40 GPa with features that resemble pyritelike optical modes [Fig. 2(a)(iii)]. Subsequent decompression after the return of the Raman signal leads to the eventual split of the main feature relating to a S–S stretching mode split into three distinct features. The reemergence of the Raman signal is highly dependant on deviatoric stress in the sample; in the case of quasihydrostatic compression in He, Raman activity is not registered up to 70 GPa.

Synchrotron x-ray diffraction reveals a transformation at 36 GPa to a-MnS_2, following a giant volume collapse of ~20%, as previously reported [15]. This structural transition remarkably is confirmed here at room temperature, while previously the high density ground-state arsenopyrite phase was reported via laser heating above 1500 K at 12 GPa [15]. This significant difference in conditions is (Fig. 4), in part, driven by deviatoric stress from the nonhydrostatic conditions of this experiment and most likely a negative Clausius–Clapeyron slope of the phase boundary. Upon decompression the system undergoes a back transformation to the ambient pyrite structure at 5 GPa.

At 40 GPa, electrical resistance was measured in between successive laser heating intervals, resulting in a decrease in conductivity. This corresponds to the reduction in the phase coexistence, with a diminishing fraction of the pyrite-like MnS_2, arising from kinetic hindrance. Upon decompression, a reemergence of the main pyrite Raman peak is observed; the A_g stretching feature at 480 cm^{-1} by ambient pressure. There is also a feature present in all Raman spectra taken during transport measurements, both on compression and decompression; this feature appears around 700–800 cm^{-1}. The origin of this feature is not identified.

Like with other Mn compounds, the transition to the low-spin phase of MnS_2 under pressure is accompanied

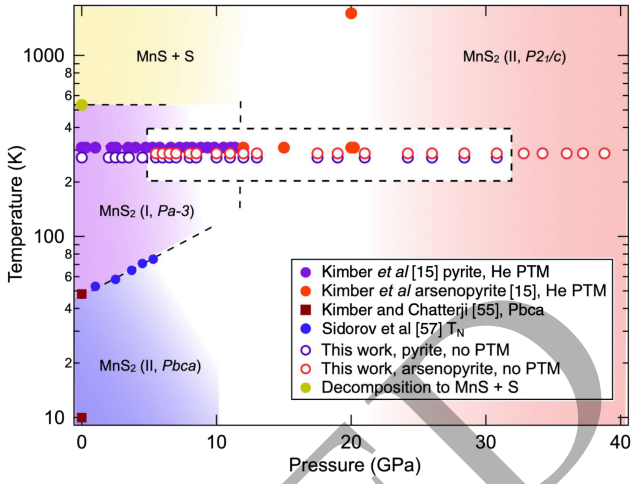

FIG. 4. T-P phase diagram of MnS_2. Until around 12 GPa, the pyrite phase is sensitive to decomposition to MnS + S through additional heat. Purple data points track pyrite $Pa\bar{3}$ MnS_2 to around 12 GPa, where $P2_1/c$ is accessible via laser heating (shown by red data points) [15]. Blue data points track the Néel temperature as a function of pressure [57], separating the AFM $Pbca$ phase [55] from the paramagnetic pyrite phase.

by a giant volume collapse [15,16,58]. An increased crystal field splitting from the initial weak field of the octahedrally coordinated S_2^{2-} ions eventually favors a low-spin configuration occupying just the Mn t_{2g} orbitals over half-occupancy of all 5 Mn^{2+} d orbitals, thus triggering the transformation into the arsenopyrite phase [15,27]. At the pressures previously examined (0–20 GPa), high temperature is necessary to drive high-spin pyrite MnS_2 into the ground, low-spin arsenopyrite phase. Prior to heating there is a disordered intermediate phase with the same oxidation state as both the pyrite and arsenopyrite phases and a XANES spectrum similar to the laser annealed arsenopyrite phase [31]. The formation of the low-spin arsenopyrite phase entails the formation of Mn–Mn bonds remarked by alternating short-long Mn–Mn distances along $[\bar{1}01]$. These Mn–Mn bonds do not result in metallization of the system unlike the two-dimensional honeycomb antiferromagnets $MnPS_3$ and $MnPSe_3$, where Mn–Mn metallic bonds formed under high pressure result in a semimetal [59].

DFT confirms that by 20 GPa of hydrostatic pressure antiferromagnetic a-MnS_2 is the true ground state structure. This was checked by both homologue optimizations and a nonspin polarized crystal structure search at 50 GPa. The proposed marcasite ($Pnnm$, m-MnS_2) structure was also evaluated in detail in a nonspin polarized, ferromagnetic (FM), and AFM (magnetic polarization following [001]) form [60,61]. The 0, 11, 20, and 50 GPa optimized structures for m-MnS_2 are nearly identical to those of a-MnS_2 with a consistent preferred energy ordering of AFM > FM > nonspin polarized. In each instance, the magnetic solutions for a-MnS_2 and m-MnS_2 adopt a low-spin state with a magnetic moment around 1 μ_B; the

persevering moments indicate that even 50 GPa is not enough to form 1D metal bonded chains.

Continuing to compress high-spin AFM-III pyrite-like MnS_2 would potentially increase the MLCT enough to trigger the $Mn^{2+} + S_2^{2-} \rightarrow Mn^{4+} + 2S^{2-}$ reaction, however the metallic, high-spin phase is metastable. Beyond 40 GPa the DFT optimizations collapse into a low-spin ($S_{Mn} = 1/2$) AFM-III, orthorhombically distorted pyrite MnS_2 phase that is nonmetallic. As in a-MnS_2, the transition into low-spin AFM-III pyritelike MnS_2 is accompanied by a large volume collapse. Low-spin AFM-III pyritelike MnS_2 is 23.6% smaller than the high-spin phase at 0 GPa, and this margin narrows to 11.8% at 40 GPa. This low-spin phase becomes enthalpically more favorable than the high-spin phase at 25 GPa (ignoring vibrational free energy contributions), meaning that the observed metallic phase is metastable supported by a combination of kinetic hindrance and deviatoric stresses.

In summary, an insulator to metal transition is measured in MnS_2, with a colossal seven order drop in resistance over a modest pressure range of 12 GPa. DFT simulations indicate the metallization occurs via unoccupied S_2^{2-} σ^*_{3p} antibonding states crossing the Fermi level resulting in metal-to-ligand charge transfer. This variation of a charge transfer insulator-to-metal transition is unique to anions with unsaturated valences. Metallic MnS_2 transforms into the arsenopyrite structure at 36 GPa, and that transformation is accompanied by a giant volume collapse arising from a high-to-low spin transformation of the Mn^{2+} ions. Transformation into the arsenopyrite phase returns MnS_2 to an insulator as is confirmed by resistance measurements and DFT. These results are not only pertinent to understanding manganese dichalcogenides, but also in establishing a better understanding of the electron correlation effects in related materials. In particular, this includes systems with molecular anions and across the group 7 elements where electron correlation effects produce very different structures for materials of similar composition [62].

We thank Tapan Chatterji for discussions and the original sample. This material is based upon work supported by the National Science Foundation, Division of Materials Research under Grant No. 1904694. N. D.-G., E. S., and R. P. D. were supported by NSF, Grant No. DMR-1809649; DOE Stockpile Stewardship Academic Alliance Program, Grant No. DE-NA0003898; and U.S. Department of Energy, Office of Science, Fusion Energy Sciences under Award No. DE-SC0020340. S. A. J. K. was supported by Contract No. ANR-15-IDEX-0003. Computational resources provided by the UNLV National Supercomputing Institute. Portions of this work were performed at HPCAT (Sector 16), Advanced Photon Source (APS), Argonne National Laboratory. HPCAT operations are supported by DOE-NNSA's Office of Experimental Sciences. The Advanced Photon Source is a U.S. Department of Energy (DOE) Office of Science User Facility operated for the DOE Office of Science by Argonne National Laboratory under Contract No. DE-AC02-06CH11357.

*keith.lawler@unlv.edu
†rdias@rochester.edu
‡salamat@physics.unlv.edu
§Present address: Department of Physics & Astronomy, University of Rochester, Rochester, New York 14627, USA

[1] N. F. Mott, Rev. Mod. Phys. **40**, 677 (1968).
[2] J. Zaanen, G. A. Sawatzky, and J. W. Allen, Phys. Rev. Lett. **55**, 418 (1985).
[3] M. Imada, A. Fujimori, and Y. Tokura, Rev. Mod. Phys. **70**, 1039 (1998).
[4] M. P. Pasternak, G. K. Rozenberg, G. Y. Machavariani, O. Naaman, R. D. Taylor, and R. Jeanloz, Phys. Rev. Lett. **82**, 4663 (1999).
[5] A. G. Gavriliuk, V. V. Struzhkin, I. S. Lyubutin, S. G. Ovchinnikov, M. Y. Hu, and P. Chow, Phys. Rev. B **77**, 155112 (2008).
[6] A. G. Gavriliuk, I. A. Trojan, and V. V. Struzhkin, Phys. Rev. Lett. **109**, 086402 (2012).
[7] H. Luo, R. G. Greene, K. Ghandehari, T. Li, and A. L. Ruoff, Phys. Rev. B **50**, 16232 (1994).
[8] Z. Du, S. Yang, S. Li, J. Lou, S. Zhang, S. Wang, B. Li, Y. Gong, L. Song, X. Zou, and P. M. Ajayan, Nature (London) **577**, 492 (2020).
[9] T. Bither, C. Prewitt, J. Gillson, P. Bierstedt, R. Flippen, and H. Young, Solid State Commun. **4**, 533 (1966).
[10] H. Wang, H. Yuan, S. Sae Hong, Y. Li, and Y. Cui, Chem. Soc. Rev. **44**, 2664 (2015).
[11] X.-C. Pan, X. Chen, H. Liu, Y. Feng, Z. Wei, Y. Zhou, Z. Chi, L. Pi, F. Yen, F. Song, X. Wan, Z. Yang, B. Wang, G. Wang, and Y. Zhang, Nat. Commun. **6**, 7805 (2015).
[12] L. Zhu, J. Zhou, Z. Guo, and Z. Sun, J. Materiomics **1**, 285 (2015).
[13] M. Xu, Y. Q. Cheng, L. Wang, H. W. Sheng, Y. Meng, W. G. Yang, X. D. Han, and E. Ma, Proc. Natl. Acad. Sci. U.S.A. **109**, E1055 (2012).
[14] P. Vulliet, J. P. Sanchez, D. Braithwaite, M. Amanowicz, and B. Malaman, Phys. Rev. B **63**, 184403 (2001).
[15] S. A. J. Kimber, A. Salamat, S. R. Evans, H. O. Jeschke, K. Muthukumar, M. Tomi, F. Salvat-Pujol, R. Valenti, M. V. Kaisheva, I. Zizak, and T. Chatterji, Proc. Natl. Acad. Sci. U.S.A. **111**, 5106 (2014).
[16] Y. Wang, L. Bai, T. Wen, L. Yang, H. Gou, Y. Xiao, P. Chow, M. Pravica, W. Yang, and Y. Zhao, Angew. Chem. Int. Ed. **55**, 10350 (2016).
[17] M. S. Torikachvili, S. L. Bud'ko, N. Ni, and P. C. Canfield, Phys. Rev. Lett. **101**, 057006 (2008).
[18] W. Yu, A. A. Aczel, T. J. Williams, S. L. Bud'ko, N. Ni, P. C. Canfield, and G. M. Luke, Phys. Rev. B **79**, 020511(R) (2009).
[19] A. I. Goldman, A. Kreyssig, K. Prokeš, D. K. Pratt, D. N. Argyriou, J. W. Lynn, S. Nandi, S. A. J. Kimber, Y. Chen, Y. B. Lee, G. Samolyuk, J. B. Leão, S. J. Poulton, S. L. Bud'ko, N. Ni, P. C. Canfield, B. N. Harmon, and R. J. McQueeney, Phys. Rev. B **79**, 024513 (2009).

[20] A. P. Nayak, S. Bhattacharyya, J. Zhu, J. Liu, X. Wu, T. Pandey, C. Jin, A. K. Singh, D. Akinwande, and J.-F. Lin, Nat. Commun. **5**, 3731 (2014).

[21] D. Zhou, Y. Zhou, C. Pu, X. Chen, P. Lu, X. Wang, C. An, Y. Zhou, F. Miao, C.-H. Ho, J. Sun, Z. Yang, and D. Xing, npj Quantum Mater. **2**, 19 (2017).

[22] R. P. Dias, C.-S. Yoo, M. Kim, and J. S. Tse, Phys. Rev. B **84**, 144104 (2011).

[23] M. Kim, R. Dias, Y. Ohishi, T. Matsuoka, J.-Y. Chen, and C.-S. Yoo, Sci. Rep. **6**, 31594 (2016).

[24] E. Snider, N. Dasenbrock-Gammon, R. McBride, M. Debessai, H. Vindana, K. Vencatasamy, K. V. Lawler, A. Salamat, and R. P. Dias, Nature (London) **586**, 373 (2020).

[25] G. Brostigen and A. Kjekshus, Acta Chem. Scand. **24**, 2993 (1970).

[26] T. Chattopadhyay, T. Brückel, and P. Burlet, Phys. Rev. B **44**, 7394 (1991).

[27] A. Rohrbach, J. Hafner, and G. Kresse, J. Phys. Condens. Matter **15**, 979 (2003).

[28] G. I. Csonka, J. P. Perdew, A. Ruzsinszky, P. H. T. Philipsen, S. Lebègue, J. Paier, O. A. Vydrov, and J. G. Ángyán, Phys. Rev. B **79**, 155107 (2009).

[29] S. L. Dudarev, G. A. Botton, S. Y. Savrasov, C. J. Humphreys, and A. P. Sutton, Phys. Rev. B **57**, 1505 (1998).

[30] L. Wang, T. Maxisch, and G. Ceder, Phys. Rev. B **73**, 195107 (2006).

[31] D. Durkee, D. Smith, R. Torchio, S. Petitgirard, R. Briggs, I. Kantor, S. R. Evans, T. Chatterji, T. Irifune, S. Pascarelli, K. V. Lawler, A. Salamat, and S. A. Kimber, J. Solid State Chem. **269**, 540 (2019).

[32] See Supplemental Material at http://link.aps.org/supplemental/10.1103/PhysRevLett.127.016401 for XRD pressure-volume measurements as well as additional simulation details and results, which includes Refs. [33–47].

[33] P. Hohenberg and W. Kohn, Phys. Rev. **136**, B864 (1964).

[34] W. Kohn and L. J. Sham, Phys. Rev. **140**, A1133 (1965).

[35] J. D. Pack and H. J. Monkhorst, Phys. Rev. B **16**, 1748 (1977).

[36] P. E. Blöchl, Phys. Rev. B **50**, 17953 (1994).

[37] A. M. Ganose, A. J. Jackson, and D. O. Scanlon, J. Open Source Softw. **3**, 717 (2018).

[38] A. R. Oganov and C. W. Glass, J. Chem. Phys. **124**, 244704 (2006).

[39] R. E. Bell and R. E. Herfert, J. Am. Chem. Soc. **79**, 3351 (1957).

[40] R. G. Dickinson and L. Pauling, J. Am. Chem. Soc. **45**, 1466 (1923).

[41] H. H. Murray, S. P. Kelty, R. R. Chianelli, and C. S. Day, Inorg. Chem. **33**, 4418 (1994).

[42] H.-J. Lamfers, A. Meetsma, G. Wiegers, and J. de Boer, J. Alloys Compd. **241**, 34 (1996).

[43] W. H. Baur and A. A. Khan, Acta Crystallogr. Sect. B **27**, 2133 (1971).

[44] R. Sabatini, T. Gorni, and S. de Gironcoli, Phys. Rev. B **87**, 041108(R) (2013).

[45] J. Sun, A. Ruzsinszky, and J. P. Perdew, Phys. Rev. Lett. **115**, 036402 (2015).

[46] H. Peng, Z.-H. Yang, J. P. Perdew, and J. Sun, Phys. Rev. X **6**, 041005 (2016).

[47] J. Sun, R. C. Remsing, Y. Zhang, Z. Sun, A. Ruzsinszky, H. Peng, Z. Yang, A. Paul, U. Waghmare, X. Wu, M. L. Klein, and J. P. Perdew, Nat. Chem. **8**, 831 (2016).

[48] L. M. Corliss, N. Elliott, and J. M. Hastings, J. Appl. Phys. **29**, 391 (1958).

[49] J. M. Hastings, N. Elliott, and L. M. Corliss, Phys. Rev. **115**, 13 (1959).

[50] J. Zaanen, G. A. Sawatzky, and J. W. Allen, Phys. Rev. Lett. **55**, 418 (1985).

[51] T. Mizokawa, H. Namatame, A. Fujimori, K. Akeyama, H. Kondoh, H. Kuroda, and N. Kosugi, Phys. Rev. Lett. **67**, 1638 (1991).

[52] Q. Liu, G. M. Dalpian, and A. Zunger, Phys. Rev. Lett. **122**, 106403 (2019).

[53] V. Bisogni, S. Catalano, R. J. Green, M. Gibert, R. Scherwitzl, Y. Huang, V. N. Strocov, P. Zubko, S. Balandeh, J.-M. Triscone, G. Sawatzky, and T. Schmitt, Nat. Commun. **7**, 13017 (2016).

[54] P. C. Rogge, R. U. Chandrasena, A. Cammarata, R. J. Green, P. Shafer, B. M. Lefler, A. Huon, A. Arab, E. Arenholz, H. N. Lee, T.-L. Lee, S. Nemšák, J. M. Rondinelli, A. X. Gray, and S. J. May, Phys. Rev. Mater. **2**, 015002 (2018).

[55] S. A. J. Kimber and T. Chatterji, J. Phys. Condens. Matter **27**, 226003 (2015).

[56] T. Chatterji, in *Neutron Scattering from Magnetic Materials*, edited by T. Chatterji (Elsevier Science, Amsterdam, 2006), pp. 25–91.

[57] V. A. Sidorov, J. Guo, L. Sun, and V. V. Brazhkin, JETP Lett. **107**, 311 (2018).

[58] H. Fjellvåg, A. Kjekshus, T. Chattopadhyay, H. Hochheimer, W. Hönle, and H. V. Schnering, Phys. Lett. **112A**, 411 (1985).

[59] Y. Wang, J. Ying, Z. Zhou, J. Sun, T. Wen, Y. Zhou, N. Li, Q. Zhang, F. Han, Y. Xiao, P. Chow, W. Yang, V. V. Struzhkin, Y. Zhao, and H. K. Mao, Nat. Commun. **9**, 1914 (2018).

[60] T. Chattopadhyay and H. von Schnering, J. Phys. Chem. Solids **46**, 113 (1985).

[61] T. Chattopadhyay, H. von Schnering, and W. Grosshans, Physica (Amstetrdam) **139(B+C)–140(B+C)**, 305 (1986).

[62] K. V. Lawler, B. C. Childs, D. S. Mast, K. R. Czerwinski, A. P. Sattelberger, F. Poineau, and P. M. Forster, Inorg. Chem. **56**, 2448 (2017).